



Graph attention network-based mineral prospectivity prediction: A case study of copper exploration in eastern Tien Shan, China



Shiting Sheng^a, Yongzhi Wang^{a,b,c,*}, Jiangtao Tian^c, Xingyu Chen^a, Yan Ning^a, Yuhao Dong^a

^a College of Geoexploration Science and Technology, Jilin University, Changchun 130026, China

^b Institute of Integrated Information for Mineral Resources Prediction, Jilin University, Changchun 130026, China

^c Xinjiang Academy of Geological Research, Urumqi, Xinjiang 830057, China

ARTICLE INFO

Keywords:

Graph attention network
Mineral prospectivity mapping
Copper exploration
Geological knowledge-driven

ABSTRACT

Traditional mineral prospectivity mapping (MPM) primarily relies on pixel-based analysis, which can exclude critical spatial patterns associated with mineralization. Through the attention mechanism, the Graph Attention Network (GAT) dynamically adjusts the weights between nodes, more accurately capturing the relationships between geological features. To enable intelligent copper prospectivity modeling, this study proposes integrating geological knowledge and graph neural networks. Using geological structure, metallogenic stratigraphy, and geochemical exploration data from the eastern Tien Shan orogenic belt, we constructed a unified data format and storage structure. We extract and fuse features related to copper mineralization, compile a training dataset, and apply the GAT algorithm to develop a comprehensive intelligent prediction model, Geoscientific Graph Attention Network (GeoGAT). Results indicate that the model effectively extracts features from multi-source geological data. It quantifies the suitability of prospective zones, achieving 83.3 % accuracy in identifying known copper deposits. Notably, it successfully detects numerous large known deposits. In comparative analyses with convolutional neural network (CNN) and multilayer perceptron (MLP) models, the GeoGAT model excels in assessing geological feature relevance and prediction accuracy. This study validates the effectiveness of the GAT algorithm in mineral prediction and highlights the application of graph attention networks as a frontier approach. Further exploration of their applications in mineral prediction is recommended.

1. Introduction

Mineral resource prediction is a key challenge in geological exploration. Its accuracy affects exploration feasibility and economic viability. Deep learning has emerged as a new approach that uses multi-source geoscientific data, such as geological, geochemical, geophysical, and remote sensing data (Nykänen et al., 2023; Yan et al., 2023; Zuo et al., 2015). However, traditional methods like convolutional neural networks (CNNs) have limitations. CNNs need fixed-size grid inputs and struggle with complex geological structures, like fault networks and 3D mineral distributions (Fan et al., 2023; Li et al., 2018; Zuo et al., 2024). Multilayer perceptrons (MLPs) also miss spatial mineralization patterns due to a lack of spatial correlation awareness (Fahimeh et al., 2024). Furthermore, CNNs are “black-box” models that make it difficult to interpret key mineralization factors, which limits their use by geologists (Yang et al., 2024). While knowledge-driven methods use expert insights

(Xi et al., 2023), they can be subjective and lack quantification (Feng et al., 2024a; Xiao et al., 2020). To address limitations in traditional models, this study proposes an intelligent prediction framework that integrates multi-source geoscientific data with dynamic modeling of geological features.

Recent advances in mineral exploration have brought together various methods, from traditional statistics to advanced deep-learning techniques (Lin et al., 2025; Quanke et al., 2023). Conventional approaches, such as evidence weighting and logistic regression, have long been used in mineral prospectivity mapping (MPM). For example, Li et al. (2023a, b) predicted porphyry copper deposits in Tibet by analyzing geochemical anomalies and tectonic superposition. However, these methods often depend on manual feature selection, which affects efficiency and generalizability (Akbar et al., 2024; Luo et al., 2025). The introduction of CNNs marked a significant shift, allowing automated mineral recognition through grid-based data processing (Hadj and

* Corresponding author at: College of Geoexploration Science and Technology, Jilin University, Changchun 130026, China.
E-mail address: wangyongzhi@jlu.edu.cn (Y. Wang).

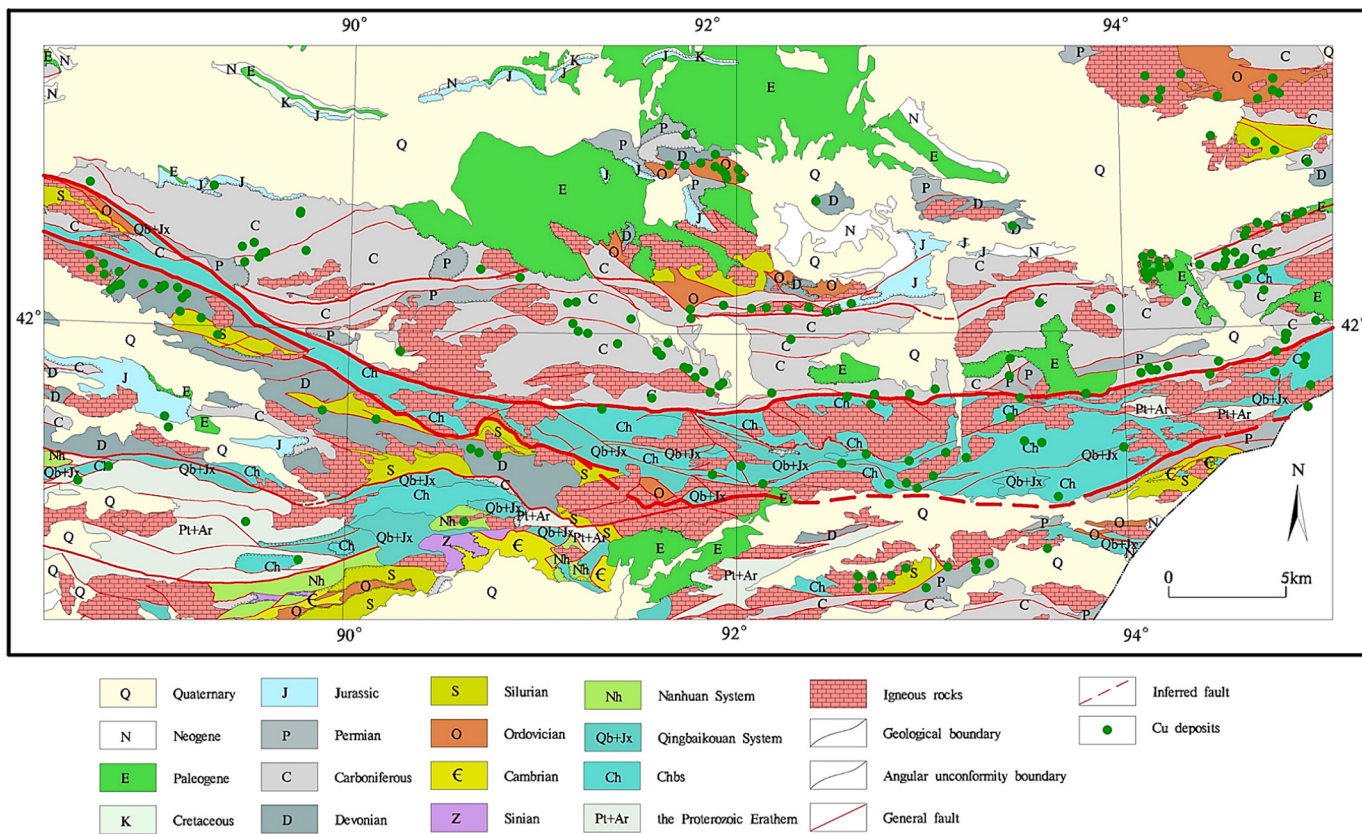


Fig. 1. Geological map of the eastern Tien Shan study area.

Wildes, 2018; Li et al., 2024). Applications range from hyperspectral image classification (Attallah et al., 2024) to remote sensing alteration extraction (Fu et al., 2023; Li et al., 2022). Yet, CNNs struggle with geological data's complex structures, failing to capture relationships among faults, lithologies, and mineralization zones (Qi et al., 2014). The layered structure of CNNs also leads to "black-box" models with limited interpretability, making them less useful in exploration workflows (Yang et al., 2024).

Graph neural networks (GNNs) offer a new way to model non-Euclidean geological systems (Ding et al., 2024). By using graph propagation with deep learning, GNNs encode topological relationships, like fault connectivity and lithological transitions, into their feature learning (Wang et al., 2025). Notable examples include graph convolutional networks (GCNs) for improved node classification (Liu et al., 2025) and hybrid CNN1D-GCN architectures for global dependency modeling (Yan et al., 2024). Despite these advances, gaps remain: (1) Most models rely on single data sources, like geophysics alone (Chudasama et al., 2024; Sihombing et al., 2024), overlooking multi-source synergy; (2) Few studies use metallogenetic theory as a constraint, leading to geologically inconsistent predictions; (3) Interpretability is often overlooked, with little focus on quantifying feature contributions.

Currently, few models combine graph neural networks with multi-source geoscience data for feature extraction and interdisciplinary information fusion. Among deep learning models, the Graph Attention Network (GAT) is a powerful spatial GNN (Velickovi et al., 2017; Zheng et al., 2023). It learns relationships between nodes and can process data in parallel, making it fast (Sihombing et al., 2024). This allows GAT to capture complex relationships in graph structures (Ye et al., 2025). The attention mechanism (Uzair et al., 2023) helps it adjust weights between nodes and update states, effectively capturing structural information (Zheng et al., 2022). It also uses a multi-head attention mechanism, which helps the model focus on different features, improving its representation and generalization abilities (Zhang et al., 2024). This makes

GAT suitable for various graph data applications.

Given these advantages, this study uses the GAT algorithm with multi-source data to predict copper mines in the eastern Tien Shan. The main contributions are:

- (1) We build a multi-source geological big data framework for the eastern Tien Shan. It includes geological structures, major ore-forming stratigraphy, and multi-element geochemical data. From this, we extract features related to copper mine prediction and create a unified data format for model training.
- (2) By considering key factors influencing copper ore formation and ore-controlling structures, we link geological knowledge with data features. We integrate the Technique for Order Preference by Similarity to the Ideal Solution (TOPSIS) with the GAT algorithm to create the GeoGAT prediction model.
- (3) We compare GeoGAT with CNN and MLP to assess prediction performance. We overlay the results with known mine site information to calculate prediction accuracy, focusing on the effectiveness and geological features of deposits like the Tuwu Copper Mine and its neighbors.
- (4) This study achieves an integrated analysis of multi-source geoscientific information, driven by data and knowledge. It enables automatic correlation across disciplines and supports intelligent copper resource prediction.

2. Overview of the study area

2.1. Geographic location of the study area

The study area is situated in eastern Xinjiang, adjacent to the southern margin of the Turpan-Hami Basin (Huang et al., 2020). It extends approximately 668 km east-west and 111 km north-south, covering a total area of 74,000 km² (Tang et al., 2022).

Geomorphologically, the region comprises the Jueluotag Mountain System along the southern basin margin, the Kawabulak and Alatalq Mountain Systems of the Middle Tianshan, and the eastern Jianshanzi, Xingxingxia, and Yirek Mountains. The area also incorporates the southern Turpan-Hami Basin, the southern Tien Shan ranges, and the northern Kuruktag terrain (Soloviev et al., 2024).

The area features low-to-medium elevation hills and mountains. Elevations range from 1000 to 1500 m, with peaks reaching 2000 m in the eastern sector (Li et al., 2020). Local relief can exceed 200 m in fault-controlled zones, but most regions show gentle terrain with elevation changes of less than 50 m. The mountain ranges mainly align in east-west, northeast-southwest, and northwest-southeast directions (Dong et al., 2009). Surface drainage is temporary, limited to intermittent streams in intermontane valleys.

The climate is hyperarid and continental, with extreme seasonal differences. Summer temperatures peak at 35–49 °C, leading to intense evaporation of over 3000 mm per year. In contrast, winter temperatures can drop to –30 °C. The mean annual precipitation is 48 mm, mostly occurring in spring. Strong aeolian activity, especially in the western areas, causes frequent dust storms and sandy landform development.

2.2. Regional geological context

The eastern Tien Shan is in a key tectonic spot at the southern edge of the Central Asian Orogenic Belt (CAOB). This area marks the meeting point of the Junggar-Kazakhstan, Siberian, and Tarim Plates (Feng et al., 2024b). The post-Paleozoic tectonic evolution involved collisional orogeny, thermal subsidence, and episodic uplift. This process created four distinct island-arc systems from south to north: 1) Zhongtianshan Arc, 2) Aqishan-Yamansu Arc, 3) Kangurta-Huangshan Forearc Basin, and 4) Dannahu-Tousuquan Arc. These arcs are separated by three main fault systems: the Achikkuduk-Shaquanzi Fault (between Zones 1–2), Yamansu-Bitterwater Fault (between Zones 2–3), and Kangurtag-Huangshan Fault (between Zones 3–4) (Liu et al., 2017).

The Dannahu-Tousuquan Arc lies along the southern Turpan-Hami Basin, between the Dacaotan and Kangguer Faults. It is a key metallogenic belt in Xinjiang. This Devonian-Carboniferous volcanic arc has intermediate-felsic volcanic sequences mixed with volcanioclastic sediments, carbonates, and turbidites. Long-lasting Ordovician-Carboniferous magmatism led to various mineralization types, including porphyry Cu deposits like the Tuwu-Yandong ore cluster (Li et al., 2023b). Recent finds of Yandong, Dongtuwu, and Yanxi deposits show the belt's rich copper resources. Igneous rocks make up the main lithological group, and there are clear links between magmatic centers and mineralized zones, as shown in Fig. 1.

3. Data and methodology

3.1. Extraction of fault tectonics and major orogenic stratigraphy

The study area has a complex tectonic history, involving crustal rifting, terrane accretion, and collisional orogeny, resulting in significant magmatic activity. Volcanic and intrusive rocks mainly formed from the Middle-Late Paleoproterozoic to Early Mesozoic. In the Late Paleoproterozoic (Huarixi period), igneous suites are the most prominent (Mahdi and Pavlis, 1998). These rocks cover approximately 50 % of the bedrock and exhibit diverse lithologies, with intermediate-acidic types being the most common (Pang et al., 2022). This variety creates ideal conditions for copper mineralization through magma-fluid interactions.

Structural mapping reveals six main fault systems, mainly concentrated along the central parts of the Dacaotan and Kangguer Faults. Analysis of deformation shows that fault movements create localized strain fields that significantly influence copper mineralization patterns (Feng et al., 2024b). The spatial link between fault intersections and known deposits supports the idea of using fault networks as key targets

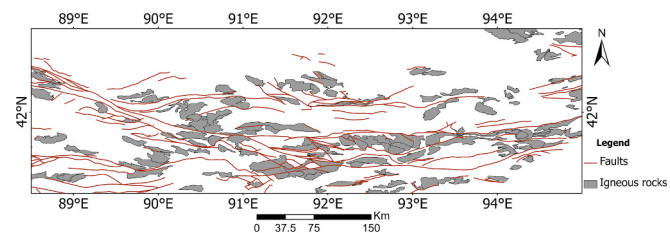


Fig. 2. Faults and igneous rocks extraction.

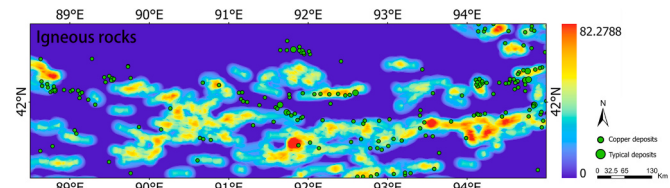


Fig. 3. Extraction of igneous rocks raster layer.

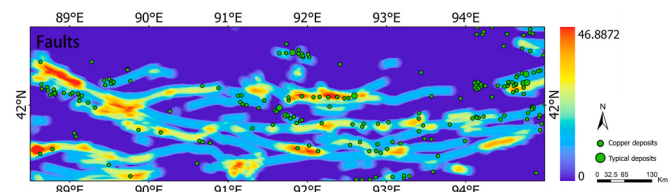


Fig. 4. Extraction of the faults raster layer.

Table 1
Correlation coefficients for each element with Cu.

Element	Correlation coefficient	Element	Correlation coefficient	Element	Correlation coefficient
Ag	0.171	La	0.135	U	0.579
As	0.441	Li	0.354	V	0.665
Au	-0.049	Mn	0.682	W	0.250
B	-0.086	Mo	0.487	Y	-0.075
Ba	0.529	Nb	0.375	Zn	0.827
Be	-0.201	Ni	0.522	Zr	0.147
Bi	0.199	P	0.288	SiO ₂	-0.487
Cd	0.471	Pb	0.260	Al ₂ O ₃	-0.375
Co	0.713	Sb	0.419	Fe ₂ O ₃	0.660
Cr	0.296	Sn	0.148	K ₂ O	-0.589
Cu	1.000	Sr	0.171	Na ₂ O	-0.551
F	0.436	Th	-0.093	CaO	0.479
Hg	0.383	Ti	0.691	MgO	0.527

for exploration (Fig. 2). We extracted raster layers of igneous rocks (Fig. 3) and faults (Fig. 4) based on the ArcGIS platform, and overlaid the known copper ore occurrence information in the study area.

3.2. Geochemical anomaly extraction

The data source is the 1:200,000 eastern Tien Shan regional chemical exploration dataset, covering 39 elements. Erroneous data were first removed to ensure a normal distribution for each element (Doherty et al., 2023). Based on the regional geological background and research needs, the target element is Cu. Therefore, based on the correlation analysis (Carranza et al., 2011) and related references search (Chen and Cheng, 2021; Grunsky and Agterberg, 1988), the elements with high correlation with Cu were selected: they are Co, Mn, Ti, V, Zn, and Fe. Correlation coefficient values are shown in Table 1.

Kriging interpolation is a statistically based interpolation method (Yan et al., 2024). It uses regionalized variables as the basis and

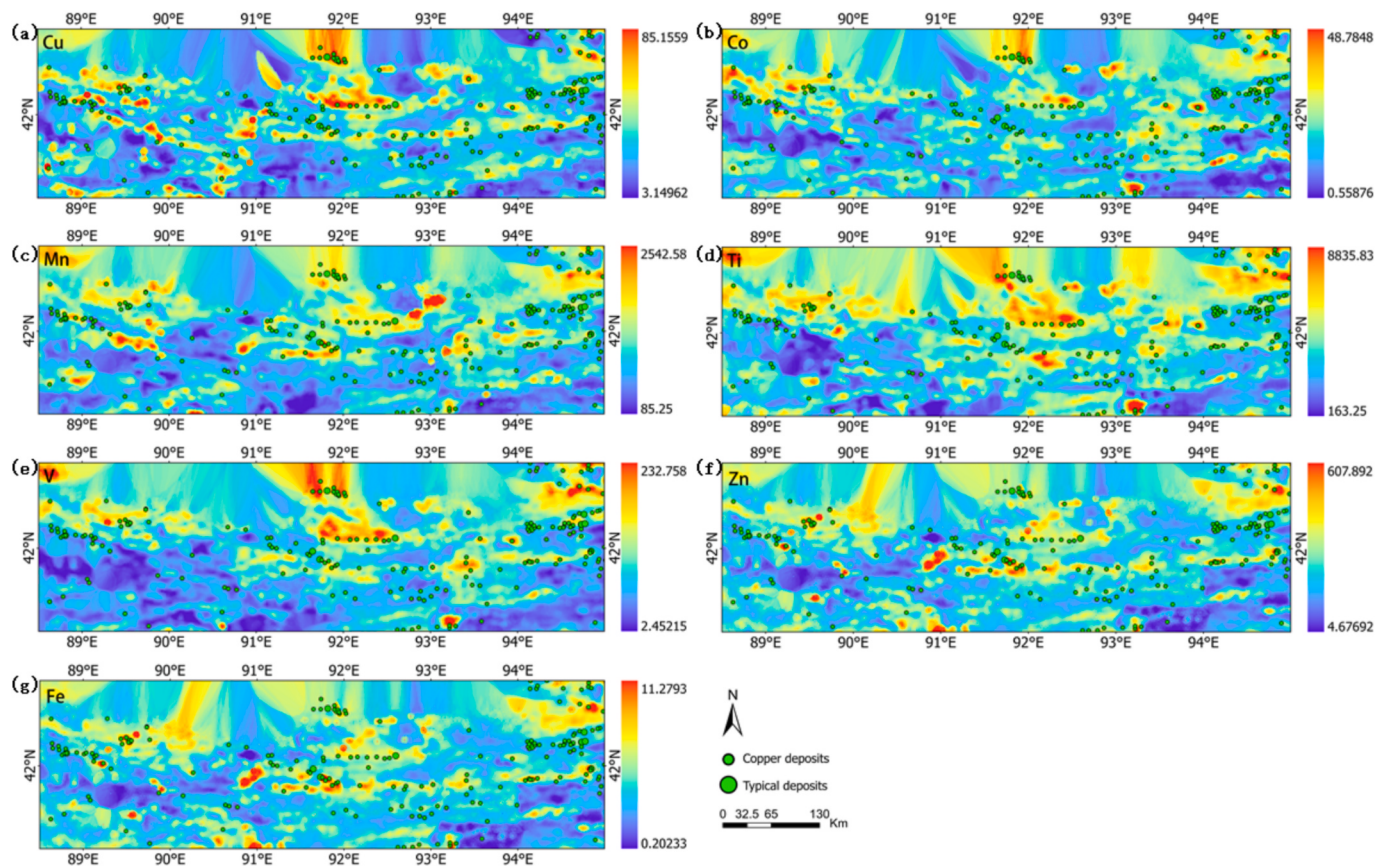


Fig. 5. Kriging interpolation to extract geochemical anomaly maps for each element: (a) Cu, (b) Co, (c) Mn, (d) Ti, (e) V, (f) Zn, (g) Fe.

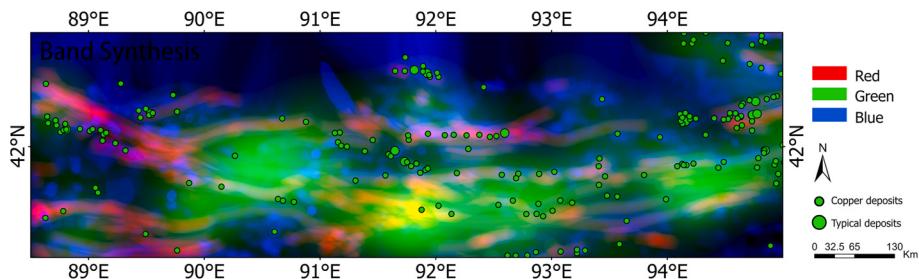


Fig. 6. Comprehensive raster layer with nine band features.

variation functions as the basic tool to perform linear unbiased and optimal estimation on unknown samples. This method has achieved good interpolation results in the field of geostatistics research. It helped interpolate the chemical exploration data for elements closely linked to copper mineralization, extracting geochemical anomaly information for each element (Juang et al., 2000). The study used the Kriging interpolation method to interpolate and analyze the geochemical data of the 7 elements mentioned above, to establish the distribution characteristics of ore-forming elements.

Overlaying with known copper deposits in the research area (Fig. 5), the results indicate that the spatial distribution similarity of Cu, Co, Mn, Ti, V, Zn, and Fe elements is high. The red color indicates areas with high geochemical anomalies, and areas with high anomalies of various ore-forming related elements often appear around copper deposits.

3.3. Integration of information on favorable elements for mineralization

Multivariate heterogeneous data were standardized into a unified format for storage and analysis. This helped extract features relevant to

fusion and copper prediction, creating a dataset suitable for model training. Using the GIS platform, raster layers of nine mineralization elements were extracted: igneous rocks, faults, Cu, Co, Mn, Ti, V, Zn, and Fe elemental anomalies. Using information from known copper deposits in the study area, we overlaid this data with the feature layers. These layers were resampled to match in image size and channel dimensions. Each layer was combined into bands, resulting in a comprehensive raster layer with nine band features (Fig. 6).

3.4. Predictive modeling

Multivariate geospatial datasets from the eastern Tien Shan were integrated through a standardized processing workflow:

1. Data Harmonization: Geological formations, metallogenic strata (igneous rocks), and geochemical anomalies (Cu, Co, Fe, Mn, Ti, V, Zn) were converted to raster format with uniform spatial resolution and coordinate system;

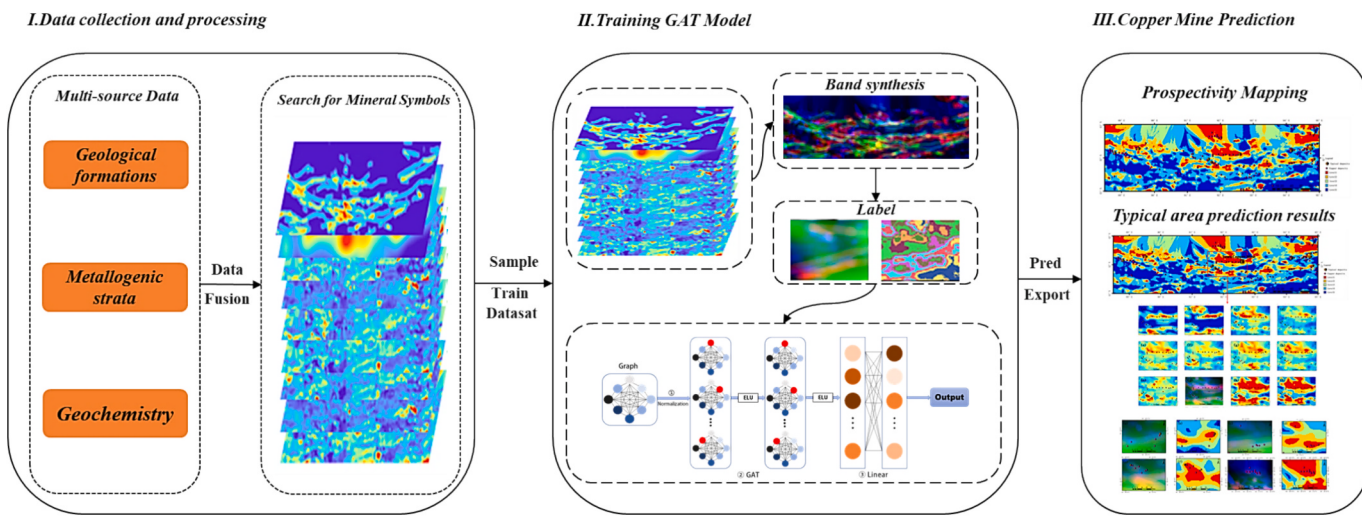


Fig. 7. Workflow of the intelligent prediction model for copper.

2. Feature Engineering: Mineralization evidence layers were resampled and synthesized through band stacking to generate composite predictor variables;
3. Dataset Partitioning: We used stratified sampling (Thomas, 2023) on the eastern Tien Shan copper mine dataset in Xinjiang (a two-dimensional table consisting of ore evidence layers and corresponding location labels), and divided the new dataset with 9 categories into training and testing sets in an 8:2 ratio (Foody et al., 1995; Zuo et al., 2023).

After training and evaluating the model, we apply it to predict copper mineralization across the study area. We assess the model's accuracy by comparing known copper occurrences with highly predictive mineralization areas. The TOPSIS algorithm optimizes factor weights, which guides the GeoGAT model towards optimal performance (Fig. 7). We implement model predictions using Python 3.8 and ArcGIS Pro.

3.4.1. TOPSIS algorithm

The TOPSIS method is a commonly used and effective approach in multi-objective decision analysis. It uses raw data to measure differences between scenarios (A. Elhassouny et al., 2016). Due to the need to process multi-source heterogeneous data and pursue interpretability of results in mineral prediction, the TOPSIS algorithm has an objective mathematical framework, an efficient calculation process, and robustness to complex data. Therefore, it can more scientifically balance subjective experience and objective data, avoid the subjective bias

problem of AHP and fuzzy methods, and become a more reliable decision-making tool. The TOPSIS process starts by normalizing the original data matrix. This gives a normalized matrix. Next, standardization removes the effects of scale differences among indicators. This creates a weight vector for factors that affect mineralization and forms a new weighted decision matrix. Each factor's weight is calculated, resulting in a refined weighted decision matrix. Then, the algorithm finds the best and worst scenarios in the dataset. It calculates the Euclidean distance for each evaluation object compared to both the best and worst scenarios. Finally, it computes how close each evaluation object is to the best option. This allows for a comprehensive evaluation of alternatives.

The most common indicators are classified into four categories: very large indicators, very small indicators, intermediate indicators, and interval indicators. To standardize indicator types, all are transformed into 'larger-is-better' indicators through indicator forwarding. For very small indicators, the conversion formula is:

$$max - x \quad (1)$$

The transformation formula for the intermediate type of indicator is as follows:

$$M = \max\{|x_i - x_{best}|\}, \tilde{x}_i = 1 - \frac{|x_i - x_{best}|}{M} \quad (2)$$

here $\{x_i\}$ is a set of intermediate-type indicator sequences, and the best value is x_{best} .

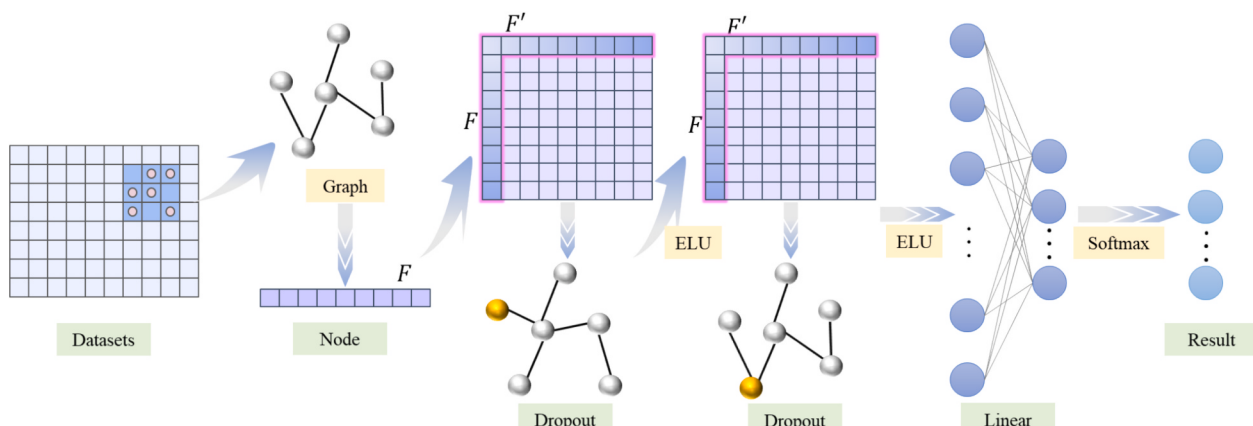


Fig. 8. Structure of the GAT.

Table 2
Model parameter settings.

Parameter	Numerical value
Attention head count	8
Dropout rate	0.2
Learning rate	1e-2
Weight decay	5e-4

The transformation of interval-type indicators is relatively complex, with a specific normalization formula:

$$M = \max\{a - \min\{x_i\}, \max\{x_i\} - b\}, \tilde{x}_i = \begin{cases} 1 - \frac{a - x_i}{M}, & x_i < a \\ 1, & a \leq x_i \leq b \\ 1 - \frac{x_i - b}{M}, & x_i > b \end{cases} \quad (3)$$

where $\{x_i\}$ is a set of interval-type indicator sequences, and the best interval is $[a, b]$.

3.4.2. GAT model construction

The TOPSIS-optimized dataset was split into two parts: a training set (80 %) and a validation set (20 %). Each feature node is a 9-dimensional vector with metallogenetic evidence parameters. The attention mechanism helps neural network models learn which features are most relevant. It focuses on key features and boosts the model's efficiency in feature extraction. When calculating each node's representation in the graph, GAT gives different weights to neighboring nodes based on their unique traits (Zhou et al., 2021). This approach addresses limitations seen in earlier methods using graph convolution or other neural networks. In each GNN layer, self-attention mechanisms adjust the weights of feature nodes and their neighbors dynamically. These weighted features go into a fully connected layer that refines them for classification, producing final predictions (Fig. 8). The specific parameter settings of the model are shown in Table 2.

The GAT model generates a new set of node features N' by inputting a set of node features (N), which can be obtained from the graph attention layer by the following steps (Zuo et al., 2023):

(1) Calculate the attention factor function as follows:

$$e_{ij} = \text{attention}(W\vec{n}_i, W\vec{n}_j) = \text{ELU}\left(\vec{a}^T [W\vec{n}_i \ W\vec{n}_j]\right) \quad (4)$$

#(4)

Where W is the weight matrix $W \in R^{F \times F}$; e_{ij} indicates the importance of node j 's features for node i ; attention is a single-layer feed-forward

neural network, and $\text{ELU}(\bullet)$ is a nonlinear activation function with a negative slope $\alpha = 0.2$.

(2) The attention coefficients were normalized using the $\text{softmax}(\cdot)$ Function (Fig. 9a).

$$\alpha_{ij} = \text{softmax}_j(e_{ij}) = \frac{\exp(e_{ij})}{\sum_{k \in N_i} \exp(e_{kj})} \quad (5)$$

(3) The final node feature vectors are calculated using a linear combination of normalized attention coefficients and the original node features.

$$\vec{n}'_i = \sigma\left(\sum_j \alpha_{ij} W\vec{n}_j\right) \quad (6)$$

In cases of nonlinear averaging, we expand the 9 mineralization evidence layers into a two-dimensional table of $n \times 9$ (where n is the number of pixels) by pixel, with each row serving as the feature data (1×9) of the corresponding node for that pixel. Use attention mechanism to calculate the weight of each node and its own and neighboring nodes (Fig. 9b), achieving adaptive weight effect through continuous training:

$$\vec{n}'_i = \sigma\left(\frac{1}{P} \sum_{p=1}^P \sum_j \alpha_{ij}^p W^p \vec{n}_j\right) \quad (7)$$

where α_{ij}^p is the normalized attention coefficient computed from the p th attention mechanism, and W^p is the weight matrix for the corresponding linear transformation in the p th attention mechanism.

3.4.3. Comparative validation of models and evaluation of indicators

This study mainly used three evaluation metrics: Receiver Operating Characteristic (ROC) curve (Xie et al., 2022), confusion matrices (Saito and Rehmsmeier, 2015), and percentage of mining sites located in the predicted area (Feng et al., 2024b).

Determine the receiver operating characteristic (ROC) of the subject by plotting a set of thresholds or critical values, where True Positive Rate (TPR) is the vertical axis of the curve and False Positive Rate (FPR) is the horizontal axis (Wen et al., 2024). The area is used to measure the accuracy of the results under the curve (ROC). The expressions for TPR and FPR are as follows:

$$TPR = \frac{TP}{TP + FN} \quad (8)$$

$$FPR = \frac{TN}{FP + TN} \quad (9)$$

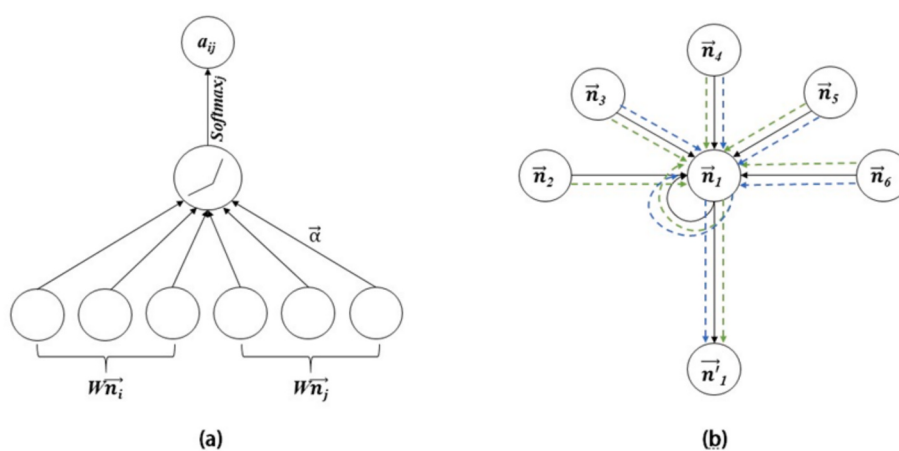


Fig. 9. GAT schematic diagram.

Table 3

Comparison of different models in terms of peak memory usage and training time.

Models	Peak Memory Usage/MB	Training Time/s
CNN	0.02	4.88
MLP	0.02	2.64
GeoGAT	0.04	5.31

TP is the true positive rate, TN is the true negative rate, FP is the false positive rate, and FN is the false-negative rate.

AUC classifies the performance of prediction models into four categories: 0.5 ~ 0.7: low effect, 0.7 ~ 0.85: average effect, 0.85 ~ 0.95: perfect effect, and 1 indicates an ideal classifier.

The confusion matrix is a visualization tool in the field of machine learning, mainly used to compare classification results with actual measured values. It can display the accuracy of classification results in a confusion matrix (Saito and Rehmsmeier, 2015). Each column represents the predicted category, and the total number of each column represents the number of data predicted for that category; Each row represents the true category to which the data belongs, and the total number of data instances in each row represents the number of instances in that category; The values in each column represent the number of predicted classes for the actual data (Zuo et al., 2021).

We measured the overlap between predicted copper zones and actual mine sites from the GeoGAT output. This overlap was measured as a proportion of all mine sites. Copper sites were classified into 'typical'

and 'common' based on existing geological data. We compared the overlap between typical copper sites and high-prediction areas for copper mines.

To highlight the GeoGAT model's performance, we compared it with two common models: CNN and MLP. Both are widely used in prediction and classification research and offer valuable references for our study. We assessed the performance of these methods for eastern Tien Shan copper mine prediction using the same training dataset as GeoGAT and the evaluation metrics mentioned earlier.

4. Results

4.1. Model performance

All experiments of this research model were conducted on a workstation (2×20 core Intel Gold 6133 CPUs, 128 GB of memory, and 48 GB of VRAM RTX 4090 GPU). The Peak Memory Usage and Training Time of the three models are shown in Table 3. The difference in training time and peak memory during training among the three models is not significant.

We evaluated the performance of each model using ROC curves and confusion matrices. The ROC curves of each model are shown in Figs. 10–12 (a), where AUC is the area under the ROC curve. GeoGAT maintained a low false positive rate and a high true positive rate in all categories of the test set. The AUC of each category exceeds 99 %, and the ROC curve usually converges towards the upper left corner of the

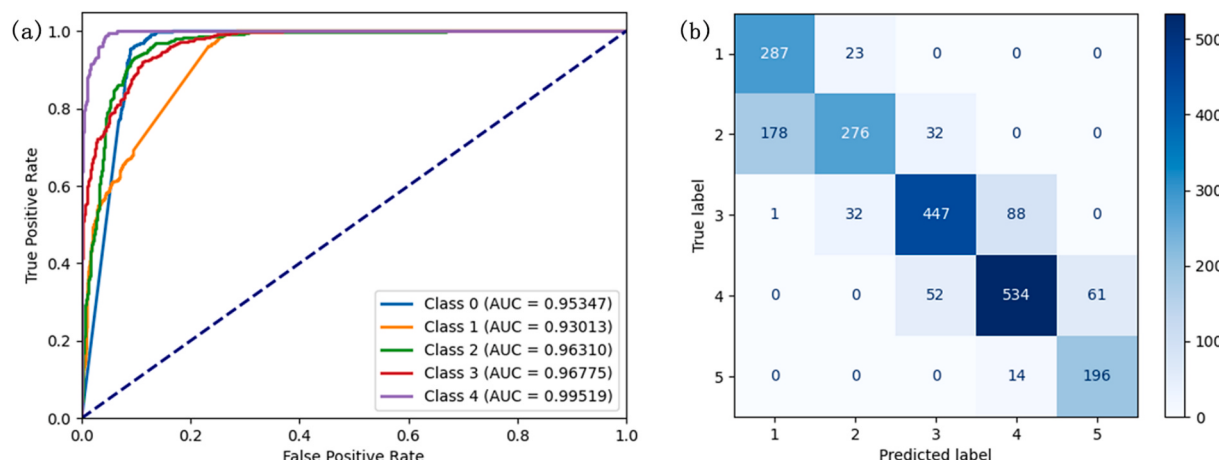


Fig. 10. ROC curves and confusion matrix of CNN: (a) ROC curve for each class, (b) the confusion matrix of CNN.

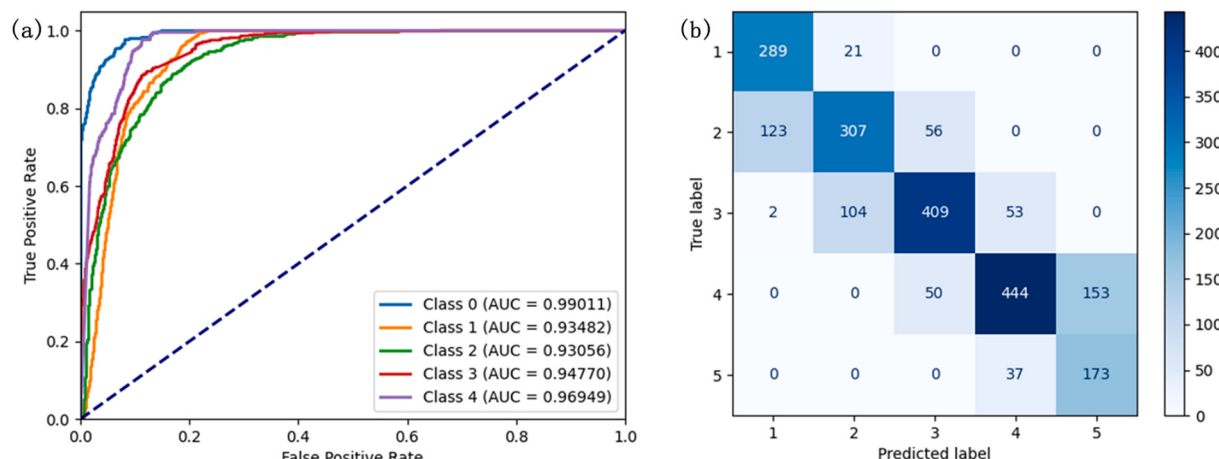


Fig. 11. ROC curves and confusion matrix of MLP: (a) ROC curve for each class, (b) the confusion matrix of MLP.

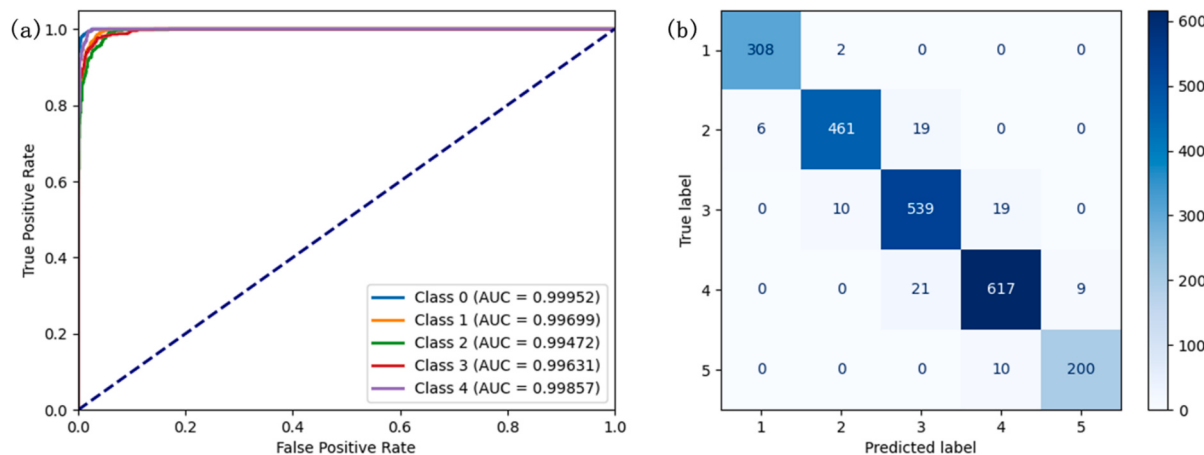


Fig. 12. ROC curves and confusion matrix of GeoGAT: (a) ROC curve for each class, (b) the confusion matrix of GeoGAT.

Table 4
Model performance comparison.

Metric	CNN	MLP	GeoGAT
Overall Accuracy	78.3 %	73.0 %	95.7 %
Macro Recall	80.8 %	75.9 %	96.2 %
Macro Precision	77.9 %	71.2 %	96.0 %
F1-Score (label 5)	83.9 %	64.6 %	95.4 %

graph, indicating that the model can accurately perform scoring tasks for different categories within the training area; In contrast, CNN has a lower true positive rate before false positives of about 0.1, and the AUC of each category is smaller than the corresponding value of GeoGAT; The true positive rate level of MLP is lower than that of CNN before the false positive rate is about 0.2, and the AUC of each category is smaller than the corresponding values of GeoGAT and CNN.

In addition, based on the confusion matrix of CNN, MLP, and GeoGAT models (Figs. 10–12 (b)), we calculated the values of Overall

Accuracy, Macro Recall, Macro Precision, and F1 Score (label 5). The results are shown in Table 4, and the GeoGAT model achieved the highest values in all indicators. In summary, the GeoGAT model has the best performance.

4.2. Model prediction results and comparative analysis

Based on the reliability of the multi-source dataset, the GeoGAT model was used to predict copper across the study area. This was compared to the CNN and MLP models. All models produced copper prediction maps (Figs. 13–15). The GeoGAT model identified a Level 1 prediction area with 33.8 % of known copper mining sites. It also found a Level 2 area with 62.3 % and a Level 3 area covering 83.3 % of the sites (Table 5). These percentages are significantly higher than those achieved by CNN and MLP models.

While CNN and GeoGAT show similar overall trends, GeoGAT's predictions are more continuous. This more accurately reflects underlying geological processes. CNN's results can be abrupt and fail to show the spatial patterns linked to mineralization. The traditional MLP model

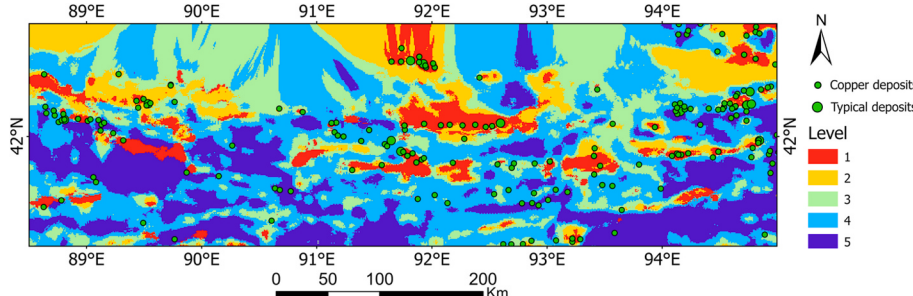


Fig. 13. CNN model copper prospectivity map.

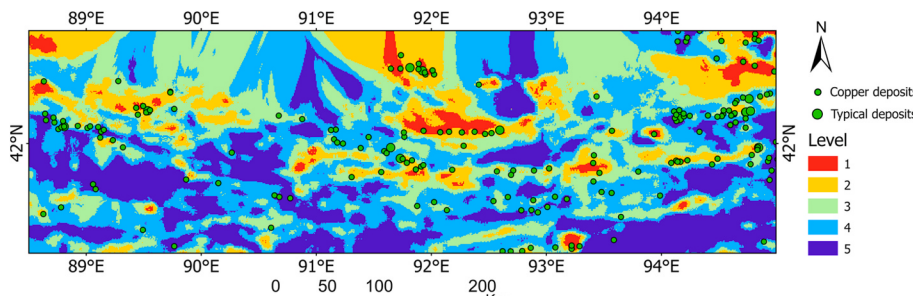


Fig. 14. MLP model copper prospectivity map.

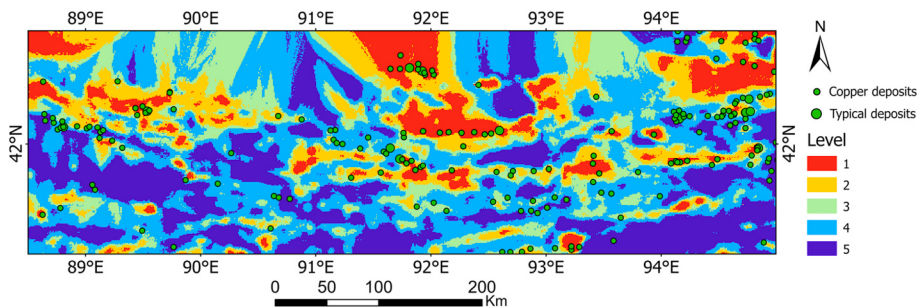


Fig. 15. GeoGAT model copper prospectivity map.

Table 5
Proportion of sites in each model prediction area.

Models	Level1	Level2	Level3
CNN	56/204 (27.4 %)	84/204 (41.2 %)	139/204 (68.1 %)
MLP	28/204 (13.7 %)	67/204 (32.8 %)	133/204 (65.2 %)
GeoGAT	69/204 (33.8 %)	127/204 (62.3 %)	170/204 (83.3 %)

only overlaps with my sites by 13.7 % in the Level 1 prediction area. Despite identifying numerous sites, the overall prediction accuracy is low.

Additionally, the GeoGAT model accurately predicts typical deposits in the eastern Tien Shan area, like the Tuwu Copper Mine, as Level 1 zones. Other sites, such as the Shaquanzi North and Xiaorequanzi copper mines, are also identified as high-prediction zones. This confirms the model's strong performance and accuracy from both theoretical and data perspectives. Thus, the GeoGAT model is more suitable for

predicting copper ore in this study. It effectively manages the spatial relationships between geological features and comprehensively predicts potential copper ore zones. This highlights its practical value and predictive reliability.

4.3. Typical area prediction results

The Tuwu Copper Mine, discovered by the Xinjiang Geology and Mining Bureau, represents a major recent advancement in the exploration of porphyry-type copper deposits. The deposit is located between the Kangurtag and Dacaotan Faults. It is one of the most important porphyry copper mines in China (An et al., 2022). The deposit lies mainly in the Carboniferous accretionary collage island arc zone at the southern edge of the Junggar Plate. The ore body exists within the Carboniferous porphyritic and dioritic granitic porphyry bodies. It features vein-dipping with considerable thickness, uniform mineralization, low grade, simple components, and clear alteration zones in the surrounding rocks. Currently, the early control of the prospective scale

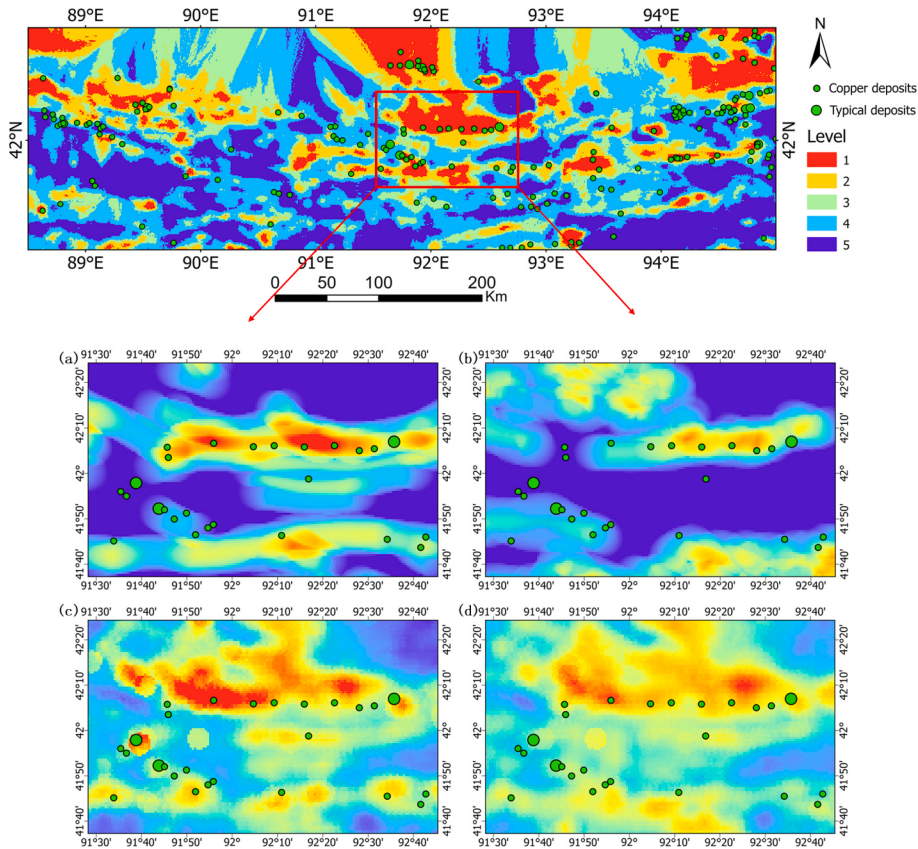


Fig. 16. Local comparative maps of the Tuwu Copper Mine and its neighbors: (a) Faults (b) Igneous rocks (c) Cu (d) Fe (e) Co (f) Mn (g) Ti (h) V (i) Zn (j) Band composites (k) Prospectivity map of Cu ore (continuous) (l) Prospectivity map of Cu ore (discrete).

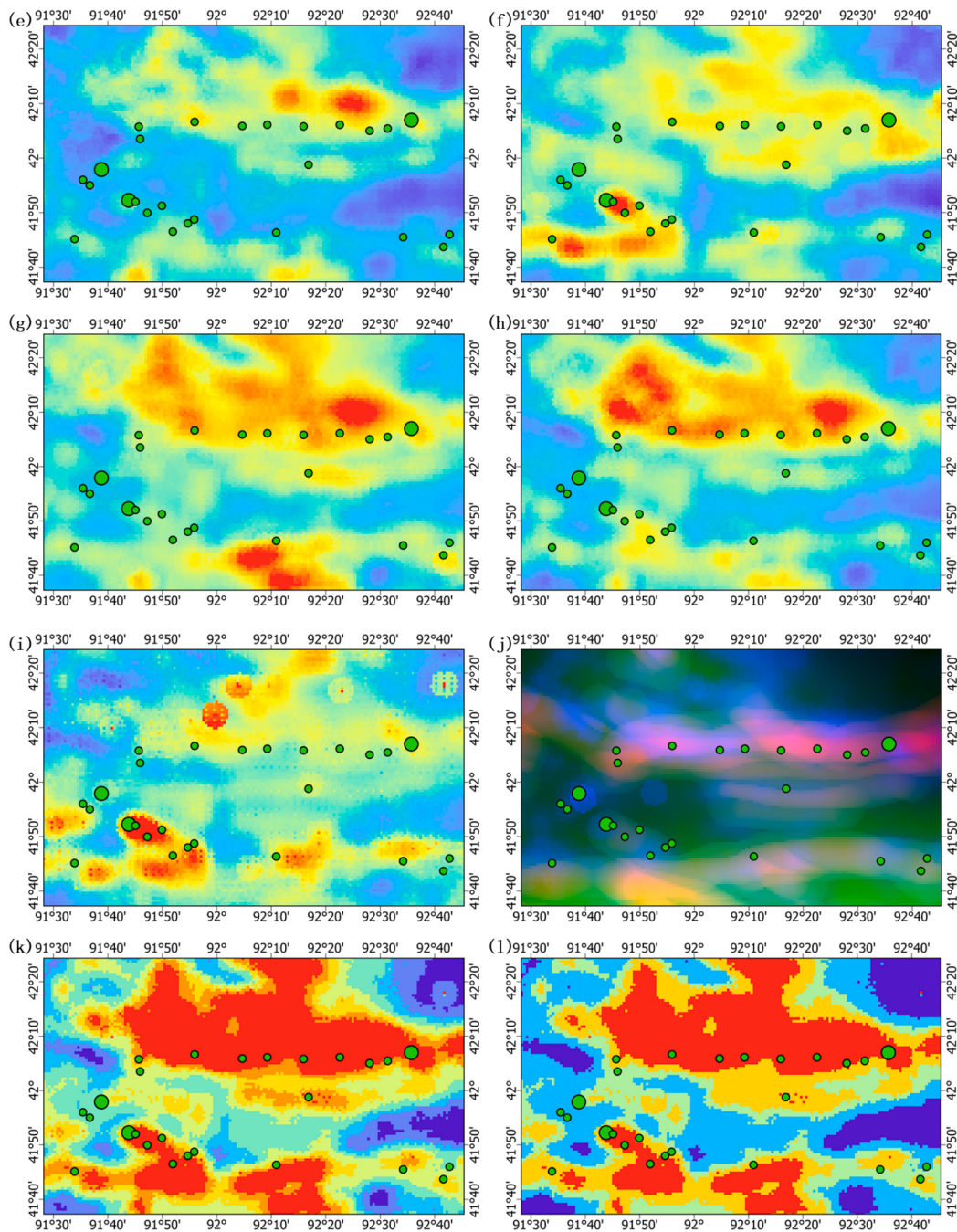


Fig. 16. (continued).

suggests it may evolve into a large-scale deposit. This discovery is crucial for guiding the search for porphyry copper ore in Xinjiang. It will also significantly boost the future growth of the mining economy in the region.

Comparing the feature layers and prediction maps of the Tuwu Copper Mine area (Fig. 16), we see highly significant geological features and geochemical anomalies. After model training, this site emerged as the top prediction area for copper mines. This indicates that it has very favorable geological features and a strong metallogenetic background. Mineral excavation can proceed in the surrounding areas, showcasing the model's effectiveness. Additionally, notable copper deposits like Shaquanzibei, Shanshan Rights, and some smaller known deposits were effectively identified through the GeoGAT model training (Fig. 17). Areas within the high prediction zone that lack known deposits can be targeted for future mineral exploration.

5. Discussion

The model performs poorly in predicting smaller mineral deposits, mainly due to the inherent limitations of 1:200,000 scale geochemical data:

- (1) The 1:200,000 scale requires a 5 km × 5 km grid sampling (International Code of Conduct [JORC Code](#), 2012). Small ore deposits typically have a length of less than 300 m and a width of less than 5 m, which can result in some small deposits falling completely between sampling points and local weak anomalies being obscured by the regional background field.
- (2) Secondly, the range of elements related to small mineral deposits is often less than 2 km ([Carranza, 2008](#)), and 1:200,000 data cannot capture such short-range variations;

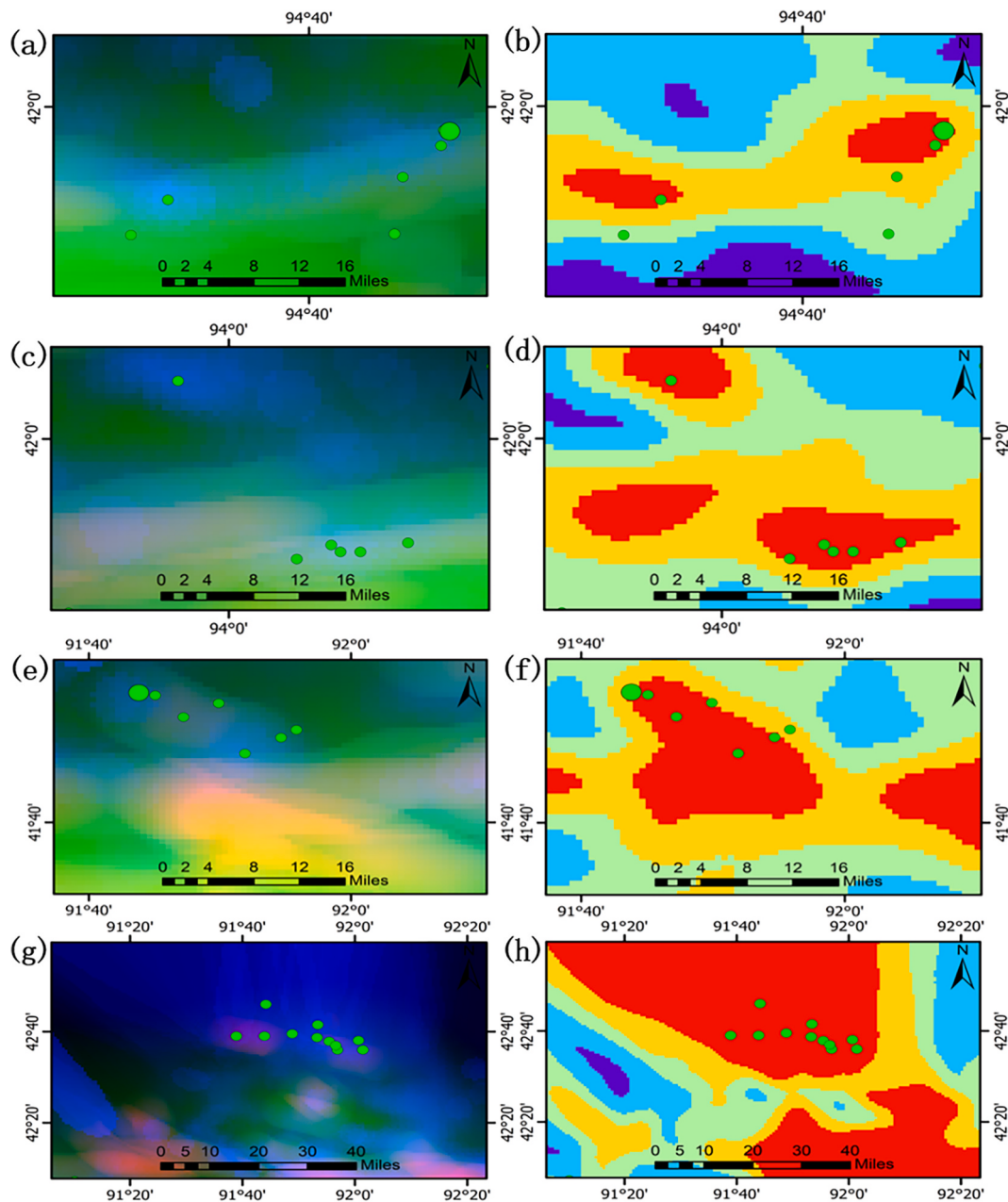


Fig. 17. Comparison maps of localized deposits: (a) RGB composite image of the Shaquanzibei copper mine area (b) Prospectivity map of the Shaquanzibei copper mine area (c) RGB composite image of the eastern localized copper mine area (d) Prospectivity map of the eastern localized copper mine area (e) RGB composite image of the Shanshan Rights copper mine area in Xinjiang (f) Prospectivity map of the Shanshan Rights copper mine area in Xinjiang (g) RGB composite image of the upper-middle localized copper mine area (h) Prospectivity map of the upper-middle localized copper mine area.

Therefore, when the original data is sparse, Kriging will produce smoothing effects, leading to the amplification of interpolation errors. Although the data quality is limited, we ensured the consistency of data quality when conducting model comparison analysis for prediction. The results showed that the GeoGAT model had higher prediction accuracy than other comparison models, proving the effectiveness of this research model.

We will strengthen our theoretical learning and geological background, pay attention to small mineral deposits in the study area in future research, and strive to collect large-scale datasets of 1:2000 and 1:10,000 around small mineral deposits.

6. Conclusion

This study focused on geological structures, metallogenic stratigraphy, and chemotaxonomy data from the eastern Tien Shan region. This data guided us in creating a unified data format and storage structure. We extracted and fused features relevant to copper ore prediction, integrating them with geological knowledge using the GAT algorithm. This work led to the development of GeoGAT, an intelligent model for predicting copper ore distribution in the area. Our conclusions are as follows:

- (1) Multi-source geological exploration data effectively captures spatial relationships between mineralization zones and geological features. This makes it a valuable resource for training

predictive models. With the attention mechanism, GAT can automatically learn and extract relationships between geological features. This enables efficient data fusion and extraction of mineralization features. We systematically collected multi-source geological data from eastern Tien Shan, covering geological structures, key ore-forming stratigraphy, and multi-element geochemical anomalies. This information was processed into a structured dataset suitable for model training.

- (2) We rasterized geological formations and major ore-forming strata, then combined them with geochemical data to train a graph-attention-based prediction model. The model accurately identified predicted ore formation areas, aligning well with the geological features of known copper mines, such as the Tuwu Copper Mine and the Shaquanzibei Copper Mine.
- (3) Compared to CNN and MLP models, GeoGAT demonstrates superior performance in identifying geological correlations and predicting copper mineralization, achieving an accuracy of up to 83.3 %. Due to its strong performance, GeoGAT can also be used for predicting other mineral resources, highlighting its universal applicability.

This study integrates multi-source geoscientific data in both a data-driven and knowledge-driven framework using graph attention networks. This approach allows for a more intelligent method of copper ore prediction. The use of graph attention networks in mineral forecasting offers a promising direction for future research.

Declaration of competing interest

The authors declare that they have no known competing financial interests or personal relationships that could have appeared to influence the work reported in this paper.

Acknowledgments

This research has been supported by a key project of the National Natural Science Foundation of China (42230810), the national key R & D Program of China (2021YFC2901801, 2023YFC2906903, 2023YFC2907105), key science & technology support project of Ministry of Natural Resources of China (ZKKJ202419) and the Geological Exploration Fund of Xinjiang Uygur Autonomous Region of China (K24-XJ009).

Data availability

Data will be made available on request.

References

- A. Elhassouny and F. Smarandache, "Neutrosophic-simplified-TOPSIS Multi-Criteria Decision-Making using combined Simplified-TOPSIS method and Neutrosophics," 2016 IEEE International Conference on Fuzzy Systems (FUZZ-IEEE), Vancouver, BC, Canada, 2016, pp. 2468-2474, doi: 10.1109/FUZZ-IEEE.2016.7738003.
- Akbar, S., Abdolmaleki, M., Ghardernejad, S., Esmaeili, K., 2024. Applying knowledge-based and data-driven methods to improve ore grade control of blast hole drill cuttings using hyperspectral imaging. *Remote Sens.* 16, 2823. <https://doi.org/10.3390/rs16152823>.
- An, W., Xue, C., Zhao, Y., Li, C., 2022. Two periods of porphyry Cu mineralization and metallogenetic implications in the Tuwu-Yandong belt (NW China), based on Re-Os systematics of molybdenite. *Minerals* 12, 1127. <https://doi.org/10.3390/min12091127>.
- Attallah, Y., et al., 2024. Optimized 3D-2D CNN for automatic mineral classification in hyperspectral images reports on Geodesy and Geoinformatics. *Sciendo* 118 (1). <https://doi.org/10.2478/rgg-2024-0017>.
- Carranza, E.J.M., 2008. Geochemical anomaly and mineral prospectivity mapping in stream sediments. In: Hale, M. (Ed.), *Handbook of Exploration and Environmental Geochemistry*, Vol. 11. Elsevier, pp. 183–217.
- Carranza, E.J.M., 2011. Analysis and mapping of geochemical anomalies using logratio-transformed stream sediment data with censored values. *J. Geochem. Explor.* 110 (2), 167–185. <https://doi.org/10.1016/j.gexplo.2011.05.007>. ISSN 0375-6742.
- Chen, Y., Cheng, Q., 2021. A deep learning-based method for relationship exploration between geochemical elements. *J. Appl. Geophys.* 194, 104320.
- Chudasama, T., Dangar, K., Gadvi, K., et al., 2024. Multivariate statistical analysis of bioavailability of heavy metals and mineral characterization in selected species of coastal flora. *Sci. Rep.* 14, 11282. <https://doi.org/10.1038/s41598-024-62201-0>.
- Ding, L., Chen, B., Zhu, Y.Z.P.D.H., 2024. Mineral prediction based on prototype learning. *Comput. Geosci.* 184. <https://doi.org/10.1016/j.cageo.2024.105540>.
- Doherty, M., Arndt, K., Chang, Z., Kelley, K., Lavin, C., 2023. Stream sediment geochemistry in mineral exploration: a review of fine-fraction, clay-fraction, bulk leach gold, heavy mineral concentrate and indicator mineral chemistry. *Geochem. Explor. Environ. Anal.* 23. <https://doi.org/10.1144/geochem2022-039>.
- Dong, Z., Li, Z., Wang, F., Zhang, M., 2009. Characteristics of atmospheric dust deposition in snow on the glaciers of the eastern Tien Shan, China. *J. Glaciol.* 55 (193), 797–804. <https://doi.org/10.3189/002214309790152393>.
- Fan, M., Xiao, K., Sun, L.i., Yang, Xu., 2023. Metallogenetic prediction based on geological-model driven and data-driven multisource information fusion: a case study of gold deposits in Xiong'ershan area, Henan Province, China. *Ore Geol. Rev.* 156, 105390. <https://doi.org/10.1016/j.oregeorev.2023.105390>. ISSN 0169-1368.
- Feng, Y., Dai, J., Bai, L., Wu, C., 2024a. Prospecting prediction for the Yulong Metallogenetic Belt in Tibet based on remote sensing alteration information and structural interpretation. *Remote Sens.* 16, 1343. <https://doi.org/10.3390/rs16081343>.
- Feng, Y., Wang, Y., Wang, C., Tian, J., Wen, S., Zhou, Y., Cheng, Y., 2024b. A fuzzy gold mineral prediction model integrating with knowledge-driven and data-driven: a case study of the Hatu region in Xinjiang, China. *Minerals* 14, 1209. <https://doi.org/10.3390/min14121209>.
- Foody, G.M., McCulloch, M.B., Yates, W.B., 1995. The effect of training set size and composition on artificial neural network classification. *Int. J. Remote Sens.* 16 (9), 1707–1723. <https://doi.org/10.1080/01431169508954507>.
- Fu, Y., Cheng, Q., Jing, L., Ye, B., Fu, H., 2023. Mineral prospectivity mapping of porphyry copper deposits based on remote sensing imagery and geochemical data in the duolong ore district, Tibet. *Remote Sens.* 15, 439. <https://doi.org/10.3390/rs15020439>.
- Grunsky, E.C., Agterberg, F.P., 1988. Spatial and multivariate analysis of geochemical data from metavolcanic rocks in the Ben Nevis area. *Ontario. Math Geol* 20, 825–861. <https://doi.org/10.1007/BF00890195>.
- Hadjji, I., Wildes, R., 2018. What Do We Understand About Convolutional Networks?. 10.48550/arXiv.1803.08834.
- Huang, Ju., Guangjian, Wu., Zhang, X., Zhang, C., 2020. New insights into particle-bound trace elements in surface snow, Eastern Tien Shan, China. *Environ. Pollut.* 267, 115272. <https://doi.org/10.1016/j.envpol.2020.115272>. ISSN 0269-7491.
- JORC, 2012. Australasian code for reporting of exploration results. *Mineral Resources and Ore Reserves*, The Joint Ore Reserves Committee.
- Juang, K.-W., Lee, D.-Y., 2000. Comparison of three nonparametric kriging methods for delineating heavy-metal contaminated soils. *J. Environ. Qual.* 29. <https://doi.org/10.2134/jeq2000.00472425002900010025x>.
- Li, B., Zhengbo, Yu., Ke, X., 2023a. One-dimensional convolutional neural network for mapping mineral prospectivity: a case study in Changba ore concentration area, Gansu Province. *Ore Geol. Rev.* 160, 105573. <https://doi.org/10.1016/j.oregeorev.2023.105573>. ISSN 0169-1368.
- Li, C., Xiao, K., Sun, L.i., Tang, R., Dong, X., Qiao, B., Dahong, Xu., 2024. CNN-transformers for mineral prospectivity mapping in the Maodeng-Baiyinchagan area, southern great Xing'an range. *Ore Geol. Rev.* 167, 106007. <https://doi.org/10.1016/j.oregeorev.2024.106007>. ISSN 0169-1368.
- Li, H., Li, X., Yuan, F., Jowitt, S.M., Dou, F., Zhang, M., Li, X., Li, Y., Lan, X., Sanming, L., Ding, W., 2022. Knowledge-driven based three-dimensional prospectivity modeling of Fe-Cu skarn deposits; a case study of the Fanchang volcanic basin, Anhui province, Eastern China. *Ore Geol. Rev.* 149, 105065. <https://doi.org/10.1016/j.oregeorev.2022.105065>. ISSN 0169-1368.
- Li, N., Yang, F., Zhang, Z., 2020. Fluid inclusions and isotope (C, H, O, S, He, and Ar) study of the Xiaobaishitou skarn W-(Mo) deposit, East Tianshan, NW China. *Ore Geol. Rev.* 122, 103520. <https://doi.org/10.1016/j.oregeorev.2020.103520>. ISSN 0169-1368.
- Li, Q., Chen, G., Luo, L., 2023b. Mineral prospectivity mapping using attention-based convolutional neural network. *Ore Geol. Rev.* 156, 105381. <https://doi.org/10.1016/j.oregeorev.2023.105381>. ISSN 0169-1368.
- Lin, Q., Zuo, R., 2025. Domain adversarial neural network for mapping mineral prospectivity. *Math. Geosci.* 57, 471–498. <https://doi.org/10.1007/s11004-024-10164-3>.
- Liu, D., Li, H., Sun, Z., Cao, Y., Wang, L., Pan, J., Han, L., Ye, X., 2017. Cenozoic episodic uplift and kinematic evolution between the Pamir and Southwestern Tien Shan. *Tectonophysics* 712–713. <https://doi.org/10.1016/j.tecto.2017.06.009>. ISSN 0040-1951.
- Liu, X., Wang, M., Zhang, J., Wang, Y., Yang, J., Cheng, J., 2025. Short-wave infrared spectroscopy studies on hydrothermal minerals for exploration of the Jiaoxi W deposit, Tibet, China. *Ore Geol. Rev.* 176, 106397. <https://doi.org/10.1016/j.oregeorev.2024.106397>. ISSN 0169-1368.
- Luo, D., Wang, T., Han, J., Niu, D., 2025. Study of three-dimensional distribution of chloride in coral aggregate concrete: a CNN-BiGRU-attention data-intelligence model driven by beluga whale optimization algorithm. *Constr. Build. Mater.* 458, 139740. <https://doi.org/10.1016/j.conbuildmat.2024.139740>. ISSN 0950-0618.
- Mahdi, H., Pavlis, G.L., 1998. Velocity variations in the crust and upper mantle beneath the Tien Shan inferred from Rayleigh wave dispersion: implications for tectonic and dynamic processes. *J. Geophys. Res.* 103, 2693–2703.

- Nykänen, V., Törmänen, T., Niiranen, T., 2023. Cobalt prospectivity using a conceptual fuzzy logic overlay method enhanced with the mineral systems approach. *Nat. Resour. Res.* 32, 2387–2416. <https://doi.org/10.1007/s11053-023-10255-8>.
- Pang, Y., 2022. Stress evolution on major faults in Tien Shan and implications for seismic hazard. *J. Geodyn.* 153–154. <https://doi.org/10.1016/j.jog.2022.101939>, 101939 ISSN 0264-3707.
- Qi, L.P., Kong, H.J., Wang, T.G., et al., 2014. An analysis of gold mineralization in Norseman-Wiluna greenstone belt, Yilgarn craton, Australia. *Geol. Bull. China* 2, 194–209.
- Quanke, L., Guoxiong, C., Lei, L., 2023. Mineral prospectivity mapping using attention-based convolutional neural network. *Ore Geol. Rev.* 156.
- Saito, T., Rehmsmeier, M., 2015. The precision-recall plot is more informative than the ROC plot when evaluating binary classifiers on imbalanced datasets. *PLoS One* 10 (3), e0118432. <https://doi.org/10.1371/journal.pone.0118432>.
- Shibombing, M.F., Palin, M.R., Hughes, S.H., et al., 2024. Improved mineral prospectivity mapping using graph neural networks. *Ore Geol. Rev.* 172106215-106215.
- Soloviev, S.G., Kryazhev, S.G., Semenova, D.V., et al., 2024. Late Paleozoic potassic intrusions of the Eastern Part of the Nikolaev Line and associated W–Mo–Cu–Au mineralization: first isotopic U–Pb zircon data (LA-ICP-MS Method) for rocks from the Adyrtor intrusions (Middle Tien Shan, Eastern Kyrgyzstan). *Dokl. Earth Sc.* 517, 1288–1296. <https://doi.org/10.1134/S1028334X24602013>.
- Tang, Q., Sun, W., Ao, S., et al., 2022. Strong lateral heterogeneities of upper mantle shear-wave structures beneath the central and eastern Tien Shan. *Int. J. Earth Sci. (geol Rundsch)* 111, 2555–2569. <https://doi.org/10.1007/s00531-021-02149-y>.
- Thomas, L. (2023, June 22). Stratified Sampling | Definition, Guide & Examples. Scribbr. Retrieved June 17, 2025, from <https://www.scribbr.com/methodology/stratified-sampling/>.
- Veliković, P., Cucurull, G., Casanova, A., et al., 2017. Graph Attention Networks. <https://doi.org/10.48550/arXiv.1710.10903>.
- Wen, S., Wang, Y., Gong, Q., Liu, J., Kang, X., Liu, H., Chen, R., Zhu, K., Zhang, S., 2024. A new robust lunar landing selection method using the bayesian optimization of extreme gradient boosting model (BO-XGBoost). *Remote Sens.* 16, 3632. <https://doi.org/10.3390/rs16193632>.
- Xi, W., Ping, Y., Tao, J., Liu, C., Shen, J., Zhang, Y., 2023. Predicting copper-polymetallic deposits in Kalatag using the weight of evidence model and novel data sources. *Open Geosci.* 15 (1), 20220588. <https://doi.org/10.1515/geo-2022-0588>.
- Xiao, F., Wang, K., Hou, W., et al., 2020. Prospectivity mapping for porphyry Cu–Mo mineralization in the Eastern Tianshan, Xinjiang, Northwestern China. *Nat. Resour. Res.* 29, 89–113. <https://doi.org/10.1007/s11053-019-09486-5>.
- Xie, L., Zhang, R., Zhan, J., Li, S., Shama, A., Zhan, R., Wang, T., Lv, J., Bao, X., Wu, R., 2022. Wildfire risk assessment in Liangshan Prefecture, China based on an integration machine learning algorithm. *Remote Sens.* 14, 4592. <https://doi.org/10.3390/rs14184592>.
- Yan, Q., Xue, L., Li, Y., Wang, R., Bo, Wu, Ding, K.e., Wang, J., 2023. Mineral prospectivity mapping integrated with geological map knowledge graph and geochemical data: a case study of gold deposits at Raofeng area, Shaanxi Province. *Ore Geol. Rev.* 161, 105651. <https://doi.org/10.1016/j.oregeorev.2023.105651>. ISSN 0169-1368.
- Yan, Q., Zhao, J., Xue, L., et al., 2024. Mineral prospectivity mapping based on spatial feature classification with geological map knowledge graph embedding: case study of gold ore prediction at Wulonggou, Qinghai Province (Western China). *Nat. Resour. Res.* 33, 2385–2406. <https://doi.org/10.1007/s11053-024-10386-6>.
- Yang, F., Zuo, R., 2024. Geologically constrained convolutional neural network for mineral prospectivity mapping. *Math. Geosci.* 56, 1605–1628. <https://doi.org/10.1007/s11004-024-10141-w>.
- Ye, Z.L., Gao, Y., Li, C., Chen, F., Xia, S., Li, Y., 2025. Prospecting model and deep mineralization predictions for the Lamasu-Saibo copper deposit based on combined geological and geophysical exploration information. *Ore Geol. Rev.* 176, 106443. <https://doi.org/10.1016/j.oregeorev.2025.106443>. ISSN 0169-1368.
- Zhang, F., Li, W., Liu, Y., Xia, Q., 2024. Resource potential evaluation of magmatic cobalt and nickel in the east Kunlun metallogenic belt, northwest of China through a geological-constrained convolutional neural network model. *Ore Geol. Rev.* 172, 106204. <https://doi.org/10.1016/j.oregeorev.2024.106204>. ISSN 0169-1368.
- Zheng, A.Y., Chen, C., Chen, Y.Q., Zhao, B.B., Zhao, P.D., 2023. Application of SVD combined with PCA in delineation and evaluation of ore-prospecting targets in the Gejiu tin polymetallic cluster region, SW China. *Ore Geol. Rev.* 160, 105571. <https://doi.org/10.1016/j.oregeorev.2023.105571>.
- Zheng, S., Song, Wu., Zheng, Y., Chen, L., Wei, C., Huang, P., Jing, X., Zaiying, Yu., He, C., Ren, H., 2022. Identifying potential porphyry copper mineralization at the Zhu'nuo ore-cluster district in western Gangdese, southern Tibet: Insights from shortwave infrared (SWIR) spectrometry and geochemical anomalies. *Ore Geol. Rev.* 151, 105202. <https://doi.org/10.1016/j.oregeorev.2022.105202>. ISSN 0169-1368.
- Zuo, R., Shi, L., Yang, F., et al., 2024. ArcMPM: an ArcEngine-based software for mineral prospectivity mapping via artificial intelligence algorithms. *Nat. Resour. Res.* 33, 1–21. <https://doi.org/10.1007/s11053-023-10286-1>.
- Zuo, R., Zhang, Z., Zhang, D., Emmanuel, J.M., Carranza, H.W., 2015. Evaluation of uncertainty in mineral prospectivity mapping due to missing evidence: a case study with skarn-type Fe deposits in Southwestern Fujian Province, China. *Ore Geol. Rev.* 71, 502–515. <https://doi.org/10.1016/j.oregeorev.2014.09.024>. ISSN 0169-1368.